Nanoscale

PAPER

View Article Online
View Journal | View Issue

Check for updates

Cite this: *Nanoscale*, 2025, **17**, 27495

Design of an RSM-optimized magnetic–fluorescent nanoprobe utilizing geothermal silica for enhanced bacterial sensing

Falah Azizah Elmaria,[a,b] Fauzan Aulia,[a,b] Shaimah Rinda Sari,[b] Sudiyarmanto,[b] Abdi Wira Septama,[c] Yuni Kusumastuti,[a] Himawan Tri Bayu Murti Petrus[a] and Siti Nurul Aisyiyah Jenie *[b]

In this study, we synthesized a magnetic fluorescent silica nanocomposite (MFSNc) using a controlled modified sol–gel method for sensitive recognition of *Staphylococcus aureus* (SA) bacteria. The effects of rhodamine B concentration, Si/Fe ratio, and percentage of cetyltrimethylammonium bromide (CTAB) on the fluorescence intensity, magnetic saturation, and specific surface area, respectively, were statistically optimized using the Box–Behnken Design within the framework of response surface methodology (RSM). This resulted in an optimized value of 5 mg g^{-1}, 0.5 g g^{-1}, and 3% of rhodamine B concentration, Fe/Si ratio, and CTAB, respectively. The RSM-optimized MFSNc generated enhanced intrinsic properties, *i.e.*, a high fluorescence intensity of 566.20 a.u. at 583.97 nm, a magnetic saturation of 16.70 emu g^{-1}, and a specific surface area of 139.45 m^2 g^{-1}. The MFSNc sample was further modified with vancomycin and applied as a biosensing platform to detect the presence of SA bacteria. After 25 minutes of incubation time, the fluorescence intensity obtained before and after SA detection was 42.59 a.u and 4.60 a.u., respectively, obtaining a decrease of intensity (%I_{loss}) of 89.20%. A linear relationship between %I_{loss} and the SA concentrations from 10^0 to 10^8 CFU mL^{-1} was observed with LOD calculated to be 5.08 CFU mL^{-1}. The sensitivity of the RSM-optimized MFSNc in detecting SA bacteria makes it suitable for applications in clinical diagnostics, food safety, and environmental monitoring.

Received 21st April 2025,
Accepted 15th October 2025

DOI: 10.1039/d5nr01610j

rsc.li/nanoscale

Published on 24 October 2025. Downloaded on 2/11/2026 1:26:59 AM.

Introduction

Among the many sources of silica, geothermal waste has shown significant potential for innovative applications in various fields. Geothermal silica originates from the deposit that circulates in the piping system of geothermal power plants. According to previous studies, these deposits consist mainly of 98.14% silica oxide (SiO_2) and other impurities, such as 0.48% phosphate oxide (P_2O_3), 0.41% potassium oxide (K_2O), and 0.29% calcium oxide (CaO).[1–3] As a result, geothermal sludge has excellent potential to be used as a precursor for the synthesis of silica nanoparticles (SiNPs). It was reported that geothermal silica can be converted into liquid silica by hydrolysis using sodium hydroxide, forming sodium silicate. When polymerized at a certain pH, sodium silicate generates SiNPs.[4] Surface chemistry is a very common method of modifying Si particles with certain functional termini, as it is regarded as one of the most versatile and reliable shell materials.

Along these lines, the modification of magnetic nanoparticles (MNPs) with silica has been used for their great potential application. MNPs are highly responsive to an external magnetic field and exhibit a high degree of relaxivity, possessing a large surface area.[5] Due to their tendency to aggregate easily,[6] MNPs are typically coated using non-magnetic materials, such as silica, in order to prevent such phenomena.[7] Silica-coated magnetic nanostructures consist of a good active side; hence, other precursors such as fluorescent agents can be added. In a previous study, Elmaria *et al.* investigated the application of geothermal silica as a coating for magnetic materials using the sol–gel method.[8] According to this study, magnetic silica materials exhibited soft-magnetic properties with a magnetization strength of 0.54 emu g^{-1}.

The bi-functional magnetic and fluorescence properties of a nanostructured system would greatly facilitate many appli-

[a]*Department of Chemical Engineering, Faculty of Engineering, Universitas Gadjah Mada, Jalan Grafika No 2, Yogyakarta, 55281, Indonesia*
[b]*Research Center for Chemistry, National Research and Innovation Agency-BRIN, Building 452, Kawasan BJ Habibie, Tangerang Selatan, Banten 15314, Indonesia. E-mail: siti043@brin.go.id*
[c]*Research Center for Pharmaceutical Ingredients and Traditional Medicine, National Research and Innovation Agency (BRIN), Kawasan Puspiptek, South Tangerang 15134, Indonesia*

Published on 24 October 2025. Downloaded on 2/11/2026 1:26:59 AM.

cations in biology and medicine, including protein purification,[9] drug delivery,[9] therapeutic sensors,[10] and biosensors.[11] The combination of magnetic and fluorescent materials gives a "two-in-one" magnetic–fluorescent material which is achieved by combining magnetic materials, such as magnetite (Fe_3O_4), maghemite (γ-Fe_2O_3), and hematite (Fe_2O_3), with fluorescent agents such as organic dyes, quantum dot semiconductors, and carbon dot materials.[10] Previous studies have utilized geothermal silica to generate silica nanomaterials incorporated with fluorescent agents as sensitive biosensing platforms for detecting antibiotic-resistant bacteria. Organic dyes such as fluorescein isothiocyanate (FITC)-modified silica have the potential as biosensors for detecting antibiotic-resistant bacteria optically, with a 77% decrease in fluorescence intensity.[12] Using geothermal silica modified with an organic dye rhodamine B, Jenie *et al.* achieved a 59.3% reduction in fluorescence when *E. coli* bacteria were present.[13] Rhodamine B offers high photostability and strong visible emission, making it a reliable fluorescent probe for optical biosensing applications.[14] While the dual properties may enhance detection sensitivity in biosensor applications,[15] the two properties could also result in side effects such as decreased fluorescence emission and magnetic field due to quenching effects.[16] A non-radiative energy transfer process is thought to be responsible for this quenching process due to fluorophore contact with the magnetic particle surfaces.[17] In this case, silica coating may hinder the quenching effect by creating a distance between the magnetic core and the fluorophore molecule.[18] Therefore, optimizing the design of precursors is essential for developing sensor materials, such as by employing response surface methodology (RSM) to identify the best conditions for synthesis and functionalization. An exciting application of magnetic–fluorescent nanomaterial systems lies in biosensing, particularly for detecting bacteria and diseases, and in drug delivery. For instance, Kavruk *et al.* developed aptamer-gated mesoporous silica nanocapsules for the targeted delivery of vancomycin to *S. aureus*, demonstrating enhanced therapeutic efficacy through controlled antibiotic release mechanisms.[19] In contrast, our approach employs a magnetic–fluorescent silica nanocomposite (MFSNc) for the direct detection of *S. aureus via* the fluorescence method, highlighting their potential as a rapid and sensitive biosensing platform in food safety and healthcare applications.

Staphylococcus aureus, commonly known as *S. aureus* (SA), is a type of Gram-positive bacteria with a round shape and arranged irregularly.[20] Samani *et al.* stated that 30% of human diseases are caused by SA bacteria without showing any symptoms.[21] The bacteria can cause severe food poisoning, and it has been identified as the causative agent in many food poisoning outbreaks. Detecting SA helps demonstrate post-processing contamination, which is often due to human contact or contaminated food-contact surfaces. The detection of SA is also important for both food and healthcare safety, as it plays an important role in preventing contamination and preserving public health. Vancomycin, a glycopeptide antibiotic, specifically targets Gram-positive bacteria such as SA by binding to the D-alanyl-D-alanine terminus of peptidoglycan precursors in their cell walls.[22] Among other materials, silica nanoparticles are commonly used for sensors due to their ease of modification. Silica-based nanoparticles exhibit a number of advantageous properties, such as being biocompatible, non-toxic, and thermally stable, which lead to a plethora of applications, including as absorbents and heterogeneous catalysts.[23] In the past few years, silica nanoparticles have been studied for their biomedical applications, and as a result, their properties have been sequentially optimized and functionalized to obtain desired properties.[5,24] In this case, silica nanoparticles were modified with vancomycin to detect SA bacteria. A study by Abdelaziz *et al.* revealed that vancomycin-conjugated magnetic nanoparticles exhibit a spherical morphology and a particle size of 16.3 ± 2.6 nm, with a silica layer of 5 nm and a total coating layer of 8 nm.[25] Sifana *et al.* reported that FITC-modified geothermal silica nanoparticles (FSiNPs) have the potential as a biosensor where the vancomycin-conjugated FSiNP material detected antibiotic-resistant bacteria *via* fluorescence quenching with a $\%I_{loss}$ of 77%.[12]

In this research, silica oxide was obtained from geothermal silica, where it served as a magnetic coating and a matrix for fluorescent agents. The precursors used for MFSNc formation include rhodamine B as a fluorescent agent, iron oxide as the magnetic core, silica oxide as the shell, and CTAB as a cationic surfactant agent. Doping fluorescent agents, such as rhodamine B, into various matrices can reduce their toxicity and enhance their photonic/chemical stability.[26] Using CTAB as a template, a large surface area can be achieved, as it is one of the most frequently used and well-established methods for enlarging the pores of mesoporous silica.[8,27] RSM based on the Design of Experiments (DoEs) was applied to optimize the precursor compositions in order to generate the MFSNc with sufficient magnetic properties and high fluorescence intensity. Among the primary categories of response surface design, the Box–Behnken Design (BBD) provides the most accurate prediction of first- and second-order coefficients as it requires fewer experiments and saves time.[28,29] Herein, we evaluate and determine the optimal composition using a three-level three-factor RSM-BBD with rhodamine B concentrations, Fe/Si ratio, and the percentage of CTAB as the independent variables to achieve the MFSNc with optimized intrinsic properties. The RSM-optimized MFSNc was then modified with vancomycin and applied as a biosensing platform for the detection of SA bacteria. This work introduces a sustainable strategy by utilizing geothermal silica as a raw material and uniquely integrates magnetic and fluorescence functionalities into a single nanostructure optimized *via* RSM. While geothermal silica has previously been explored for fluorescence-based bacterial detection,[12,13,30] this study is the first to report its use in a dual-functional magnetic–fluorescent nanocomposite specifically designed for direct sensing of *S. aureus*. The resulting vancomycin-modified MFSNc enables rapid detection of *S. aureus* through fluorescence quenching, offering a sensitive and practical biosensing platform for microbial diagnostics, contamination monitoring, and biomedical screening.

 This journal is © The Royal Society of Chemistry 2025

Published on 24 October 2025. Downloaded on 2/11/2026 1:26:59 AM.

Experimental

Materials

The geothermal precipitate was obtained from Geodipa Power Plant, Central Java, Indonesia, and used as the silica precursor. Iron(II) sulfate heptahydrate ($FeSO_4{\cdot}7H_2O$), sodium hydroxide (NaOH), ethanol, and *N*-hydroxysuccinimide (NHS) were purchased from Merck Chemicals (Darmstadt, Germany). Phosphate-buffered saline (PBS), rhodamine B (RhB), undecylenic acid, hydrochloric acid (HCl 37%), cetyltrimethylammonium bromide (CTAB), 1-(3-dimethyl aminopropyl)-3-ethylcarbodimide (EDC), vancomycin hydrochloride, and nutrient broth (NB) were purchased from Sigma-Aldrich (St Louis, MO, USA). Anhydrous iron(III) chloride salt ($FeCl_3$) was purchased from Central Drug House (P) Ltd. SA culture was provided by the National Research and Innovation Agency, BRIN. All chemicals were used without further purification, and the reagents were prepared with deionized water.

Preparation of the MFSNc and design of experiments

At first, the iron core was prepared using the co-precipitation method. 100 mL of 1.0 M $FeSO_4{\cdot}7H_2O$ and 100 mL of 0.5 M $FeCl_3$ were mixed under stirring. A black solution was produced immediately by adding NaOH. The obtained precipitate was aged at 65 °C for 30 min in an ultrasonic water bath. The samples were then washed repeatedly with deionized water and ethanol. The particles were then dried at 80 °C overnight. Then, the synthesis of sodium silicate solution was carried out following previous works by dissolving 5 g of washed geothermal silica in 200 mL of 1.5 N NaOH and mixing for 1 h at 90 °C.[8,31] The solution was then vacuum filtered to remove impurities and separate the sodium silicate solution. Using an experimental design with 15 experiments, different amounts of rhodamine B (1.25, 2.5, and 5 mg g^{-1}) were added to the sodium silicate solution and varying quantities of the iron core (2.5, 5, and 10 g) were added. The addition of 2 N HCl was carried out dropwise until a gel was formed under acidic conditions (pH 4–5). The gel was subsequently immersed in deionized water containing different concentrations of CTAB (1, 2, and 3%) at room temperature. The aging process was carried out for 18 hours at room temperature, followed by neutralization with distilled water to neutral pH. The precipitate obtained was then washed thoroughly with ethanol and deionized water to remove residual CTAB and ensure material purity and subsequently dried at 100 °C overnight. The finished product was denoted as the MFSNc.

The synthesis of the MFSNc was optimized through BBD-RSM design (Design-Expert 8.06 software, Stat-Ease Inc., Minneapolis, MN) according to the results of the three-level, three-factor experiments. The three factors were the concentration of rhodamine B, the ratio of iron oxide and geothermal silica (Fe/Si), and the concentration of CTAB as independent variables. The fluorescence intensity, magnetic saturation, and surface area as dependent variables were the outputs of this research. A set of 15 experiments was designed for the abovementioned optimization (Table S1). Using the BBD-RSM design experiment, the three levels were coded as low (−1), medium (0), and high (+1). Analysis of variance (ANOVA) was used to evaluate the quality of the fitted model. Different mathematical models (linear, two-factor interaction (2FI), quadratic, and cubic) were assessed to determine the best-fitting model based on their ANOVA descriptions. The model validation and optimization of the MFSNc nanostructures were used to determine the best formulation that may produce pure MFSNc nanoparticles with high fluorescence intensity, magnetic saturation, and surface area.

Surface modification of the MFSNc

The RSM-optimized MFSNc was further subjected to surface modification where 1 g of MFSNc was mixed with undecylenic acid until precipitated. Afterwards, the mixture of materials was reacted for 24 hours to produce MFSNc-COOH. The samples were washed with ethanol and distilled water to remove unbound undecylenic acid and dried at room temperature. Subsequently, 1 mg of MFSNc-COOH was dispersed in 1 mL of PBS solution and sonicated for 10 minutes. Further surface modification was carried out using EDC/NHS chemistry to activate carboxyl groups for efficient conjugation.[32] 10 μL of EDC (10 mg mL^{-1}) and 100 μL of NHS (5 mg mL^{-1}) were added to the samples at room temperature for 30 minutes, obtaining the MFSNc-EDC/NHS sample. To ensure the removal of unbound EDC and NHS, 10 minutes of centrifugation was performed at a speed of 10 000 rpm. Finally, 5 mg mL^{-1} of vancomycin was added to the MFSNc-EDC/NHS samples and reacted for 3 hours at room temperature. The obtained MFSNc-Van material was then washed three times with water and dispersed in PBS.

Characterization methods

Fourier Transform Infrared (FTIR) characterization was carried out using an FTIR Prestige-21 (Shimadzu, Japan) in transmittance mode at 16 cm^{-1} resolution over the range of 400–4500 cm^{-1} with an accumulating average of 10 scans. X-ray diffraction (XRD) analysis was performed using a PW1710 diffractometer manufactured by Phillips (Netherlands) with CuKα radiation at 40 kV and 30 mA, and a secondary graphite monochromator was used for the setup. The magnetic saturation was analyzed using a type 250 vibrating sample magnetometer (VSM) (Dexing Magnet Ltd, China). X-ray photoelectron spectroscopy (XPS) analyses were carried out with a Kratos AXIS Supra Plus (Kratos Analytical, Manchester, UK) spectrometer using a monochromatic Ag Kα source (10 mA, 8 kV). A Talos F200X field emission gun-transmission electron microscope (FEG-TEM, Thermo Fisher Scientific, USA) with an acceleration voltage of 200 kV and an Energy Dispersive X-ray (EDX) detector of the Super-X type was used to analyze the morphology of the synthesized MFSNc. The surface area measurement was performed using the Brunauer–Emmett–Teller (BET) method with a Tristar II 3020 Micrometrics Instrument (USA) to obtain the specific surface area at 77.3 K using a liquid nitrogen apparatus after degassing the sample at 110 °C for 6 hours. The optical density (OD)

Published on 24 October 2025. Downloaded on 2/11/2026 1:26:59 AM.

of the incubated liquid of the SA culture was determined using UV-Vis spectroscopy at a wavelength of 625 nm. Fluorescence intensity measurements were performed using a Cary Eclipse fluorescence spectrometer (Agilent, Singapore) at an excitation wavelength of 540 nm and an emission range of 500–750 nm.

Detection of *S. aureus* bacteria

SA bacteria were grown in nutrient broth (NB) media for 24 hours. A dilution of SA culture was performed to obtain a concentration of 1.5×10^8 CFU mL^{-1}. To calculate the McFarland concentration, log calculations were performed to obtain a concentration of 9.17 CFU mL^{-1} of bacteria. Then, a total of 1 mL of bacterial culture was dispersed in 900 μL of PBS and mixed with 100 μL (1 mg mL^{-1}) of MFSNc-Van solution for 1 hour. The mixture was then applied to an external magnetic field to separate the nanomaterials. After washing twice, the samples were resuspended in 100 μL of PBS.[33]

In addition to evaluating the sensor performance against SA, we also conducted comparative analyses with methicillin-resistant *Staphylococcus aureus* (MRSA). The limit of detection (LOD) was obtained by varying the concentration of SA. First, SA was detected by calculating the percentage of fluorescence intensity loss (%I_{loss}) by subtracting the maximum (I_{max}) intensity and the minimum (I_{min}) intensity. The percentage of normalized intensity was calculated using the following equation:

$$\%\ I_{loss} = \frac{I_{max} - I_{min}}{I_{max}} \times 100\% \quad (1)$$

where I_{max} and I_{min} represent the maximum fluorescence intensity of MFSNc-Van before and after detecting SA for 25 minutes of incubation. The measurements were conducted in triplicate. The standard deviation of three measurement data to plot the error bars was calculated using the following equation:

$$SD = \sqrt{\left(\sum (x_i - \bar{x})^2/(n_1)\right)} \quad (2)$$

where Σ represents the sum of all data points, x_i represents each data point, $\bar{x}$ represents the sample mean, and n represents the number of data points in the sample. Finally, the LOD was calculated using the following equation:

$$y\mathrm{LOD} = y_b + 3\mathrm{STD}_b \quad (3)$$

where y_b is the mean fluorescence intensity loss measured for the blank control and STD_b is the standard deviation.[34]

Results and discussion

Intrinsic properties of the MFSNc

In this work, an MFSNc was synthesized by modifying geothermal-based silica oxide with magnetite-type iron oxide as a core and rhodamine B as a fluorescent agent.[23] A geothermal silica precursor was used in the preparation of magnetic–fluorescent materials, which affected their physical and chemical properties. Fig. 1(a) illustrates the formation process of the MFSNc, and the success of the synthesis was confirmed based on XRD and FTIR analyses (Fig. 1(b) and (c)).

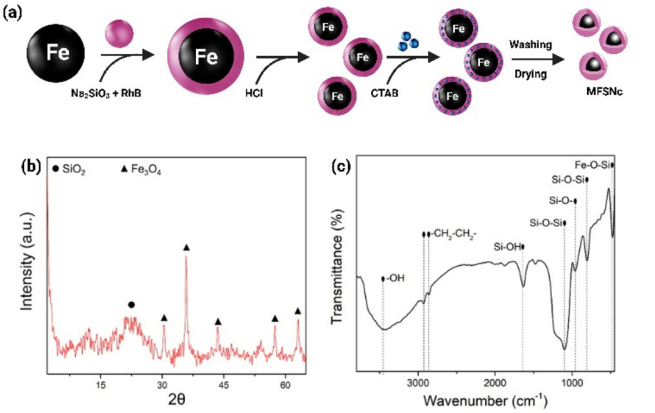

Fig. 1 (a) Schematic diagram of the formation process of the MFSNc and characteristics of the MFSNc: XRD pattern (b) and FTIR spectrum in transmittance mode (c).

As illustrated in Fig. 1(b), the XRD pattern of the MFSNc showed peak broadening at 2θ = 20–30°, indicating the presence of amorphous silica. Other diffraction patterns indicative of iron oxide in the crystalline mineral phases were observed at 2θ = 30.00°, 35.50°, 43.17°, 53.33°, and 63.00° (according to JCPDS card number 19-0629) in the form of sharp peaks, indicating a crystalline mineral. The crystallinity phase of the MFSNc material indicates the presence of an amorphous phase for silica and a crystalline phase for Fe_3O_4.[35] The FTIR spectra of the MFSNc, as shown in Fig. 1(c), exhibited absorption at 473 cm^{-1}, confirming the Si–O–Fe bond.[36,37] The identification peaks at 807 cm^{-1} and 1074 cm^{-1} corresponded to the symmetric and asymmetric vibration of siloxane groups.[29,37] The absorption peaks at 964 cm^{-1} and 1632 cm^{-1} were attributed to Si–OH bonds from symmetric and asymmetric vibrations, respectively, of silanol groups bending of water molecules.[11,31] The absorbance peaks at 2842 cm^{-1} and 2927 cm^{-1} were ascribed to $-CH_2-CH_2-$ symmetric and asymmetric vibrations, respectively, of aliphatic groups derived from the addition of rhodamine B.[13] Additionally, the broadband at around 3400–3650 cm^{-1} was assigned to O–H stretching derived from the silanol groups and the remaining absorbed water.[11,13]

According to the results of XRD and FTIR analyses, the geothermal-based silica oxide successfully coated iron oxide. The presence of two types of oxide, *e.g.*, Fe_3O_4 and SiO_2, in the XRD graph indicated the coating of SiO_2 on the iron core.[38] The presence of functional groups from silica and iron oxide in the FTIR spectra indicated that Fe_3O_4 and SiO_2 were bound covalently.[39] The core/shell structure of the nanoparticles was confirmed in our previous work[40] using Field Emission Transmission Electron Microscopy (FE-TEM), which revealed that the nanocomposite is formed with an approximate diameter of 60 nm, with the Fe_3O_4 core measuring around 40 nm. To confirm batch-to-batch reproducibility, representative TEM

 This journal is © The Royal Society of Chemistry 2025

Published on 24 October 2025. Downloaded on 2/11/2026 1:26:59 AM.

images of the current MFSNc batch are shown in the SI (Fig. S1), exhibiting consistent core–shell morphology and particle size, which is in agreement with previously reported data.

Optimization of the MFSNc

The fabrication of the MFSNc was influenced by several factors, each potentially requiring significant time for individual analysis. Consequently, traditional experimental techniques for result analysis appear inefficient and complex. Therefore, BBD-RSM experiments were used to streamline the optimization of synthesis conditions. The composition optimization design in the synthesis of the MFSNP material was conducted using the Design of Experiments (DoEs) based on the number of factors and levels used. This resulted in a three-level, three-factor DoE, leading to a total of 27 experiments. A summary was then performed using RSM, allowing 11 to 15 experiments to represent the 27 experiments. The formation of the MFSNP material utilized the BBD application on RSM for optimization. The composition formulation using RSM aimed to find the appropriate approach to connect the response function with the intended factor variables. The dependent results were analyzed to evaluate the fluorescence intensity, magnetic saturation, and surface area. Table 1 presents the experimental results' response to the calculated results of the selected mathematical model equations. This study identified the best-fit equations for the fluorescence intensity, magnetic saturation, and surface area based on BBD-RSM optimization as follows:

$$\text{Fluorescence intensity} = 96.88 + 61.86\,\text{RhB} - 64.30\,\text{Fe/Si} - 15.91\,\text{CTAB} \quad (4)$$

$$\text{Magnetic saturation} = 7.75 - 3.11\,\text{RhB} + 3.63\,\text{Fe/Si} - 1.47\,\text{Fe/Si} - 1.64\,\text{RhB Fe/Si} + 3.77\,\text{RhB CTAB} + 0.08\,\text{Fe/Si CTAB} + 6.93\,\text{CTAB}^2 - 1.76\,\text{Fe/Si}^2 + 2.51\,\text{CTAB}^2 \quad (5)$$

$$\text{Surface area} = 123.67 + 17.70\,\text{RhB} - 65.86\,\text{Fe/Si} - 82.50\,\text{CTAB} + 30.00\,\text{RhB Fe/Si} + 28.41\,\text{RhB CTAB} - 93.15\,\text{Fe/Si CTAB} \quad (6)$$

Eqn (4) illustrates a linear correlation for fluorescence intensity, with a positive RhB coefficient value of 61.86, indicating that the rhodamine B concentration is the main factor influencing fluorescence intensity. Eqn (5) and (6), which are quadratic, best describe the data related to the magnetic saturation and surface area, respectively. According to eqn (5), the dominant factor affecting magnetic strength is the Fe/Si ratio, followed by the interaction between rhodamine B concentration and CTAB concentration, as well as the squared concentrations of both. Eqn (6) reveals that the primary factor influencing the surface area is rhodamine B concentration, followed by the interaction between the Fe/Si ratio and rhodamine B concentration. The negative signs in eqn (4–6) indicate an inverse relationship between the corresponding factor levels and the response levels.[41]

The primary factors influencing this response were analyzed using a three-dimensional graph against the level of confidence (desirability), as shown in Fig. 2. According to Fig. 2A (a), CTAB did not significantly reduce the fluorescence intensity. Instead, the fluorescence intensity was primarily affected by the concentration of rhodamine B, followed by the Fe/Si ratio. Fig. 2A(b) shows that the Fe/Si ratio impacted the increase in magnetic saturation. Additionally, the Fe/Si ratio and CTAB percentage also influenced the surface area, as illustrated in Fig. 2A(c). Contour plots for each factor are presented in Fig. S2–S10. The RSM results in the synthesis of the MFSNc produced a nanocomposite with optimized fluorescence intensity, magnetic strength, and surface area. Based on the ANOVA, the optimal factors for all responses (*i.e.*, fluorescence intensity, magnetic saturation, and surface area) were identified. To ensure that the polynomial equation derived from the ANOVA

Table 1 The three-level three-factor composite design with respect to the concentration of rhodamine B, the quantity of Fe/Si, and the percentage of CTAB, as well as the actual and predicted values of the response variables (*i.e.*, fluorescence intensity, magnetic saturation, and surface area)

		Factor			FL intensity (a.u.)		Ms (emu g^{-1})		Surface area (m^2 g^{-1})	
Run #	Sample code	RhB (mg g^{-1})	Fe/Si (g)	CTAB (%)	Actual	Predicted	Actual	Predicted	Actual	Predicted
1	MFSNc-A	5	2	2	48.98	94.44	11.41	12.09	182.75	193.33
2	MFSNc-B	1.25	0.5	2	28.60	99.31	14.48	12.83	277.22	289.64
3	MFSNc-C	2.5	0.5	1	206.96	156.47	5.69	8.96	202.98	126.68
4	MFSNc-D	5	1	3	108.84	164.26	16.32	15.04	154.58	170.32
5	MFSNc-E	5	1	1	276.44	196.08	9.21	10.81	250.42	216.41
6	MFSNc-F	5	0.5	1	116.00	238.95	10.83	7.93	103.66	164.33
7	MFSNc-G	1.25	1	3	32.52	40.53	12.25	13.53	113.85	98.11
8	MFSNc-H	5	1	2	120.12	180.17	13.12	10.73	277.46	255.01
9	MFSNc-I	2.5	1	1	90.14	113.60	16.21	12.83	100.71	152.08
10	MFSNc-J	2.5	0.5	2	140.83	140.55	7.32	4.30	155.76	189.51
11	MFSNc-K	2.5	2	1	36.07	27.87	16.87	17.05	169.08	161.26
12	MFSNc-L	5	0.5	2	381.76	223.04	3.99	8.29	295.57	265.04
13	MFSNc-M	1.25	1	1	16.29	72.36	23.14	24.37	251.73	257.82
14	MFSNc-N	2.5	1	2	196.59	97.69	4.79	7.73	153.81	152.81
15	MFSNc-O	1.25	2	2	15.90	−29.28	21.95	21.09	100.69	97.92

Published on 24 October 2025. Downloaded on 2/11/2026 1:26:59 AM.

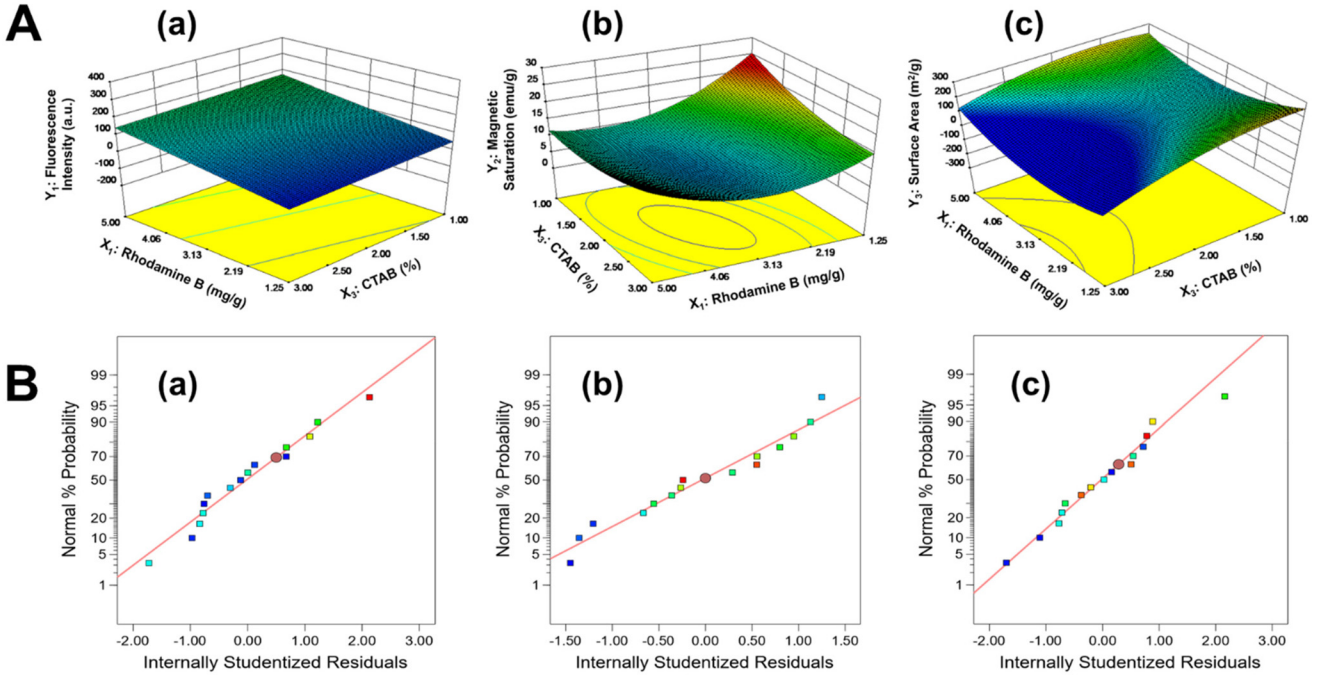

Fig. 2 Response surfaces (A) and plots of residuals (B) for each factor depicting the effect of the amount of (a) fluorescence intensity, (b) magnetic saturation, and (c) surface area.

data is reliable, further diagnostic testing is necessary. This diagnostic testing involves a normality plot graph, which compares the expected response to the actual response using a mathematical equation.

Fig. 2B confirms that the residuals for all factors (*i.e.*, fluorescence intensity, magnetic saturation, and surface area) follow a linear distribution on the normal plot graph. Consequently, the polynomial regression equations generated from the ANOVA data are deemed acceptable for predicting the optimal response for all mentioned factors.

The optimized conditions for the rhodamine B concentration, Fe/Si ratio, and CTAB concentration were determined to be 5 mg g^{-1}, 0.5 g g^{-1}, and 3%, respectively. Simultaneous optimization using RSM was employed to achieve the optimized formulation of the MFSNc based on multiple response variables. The optimized formulation should maximize the fluorescence intensity, magnetic saturation, and surface area. The responses of each parameter were calculated using their respective mathematical equations and concurrently predicted using Design Expert 8.0.6 software. One solution for the optimal conditions was generated using the software, as shown in Table 2.

The experiment results for the RSM optimum, compared with the sample data for MFSNc-F, which had the same Fe/Si ratio and rhodamine B concentration, are shown in Fig. 3. The MFSNc was designed to exhibit excellent fluorescence and magnetic properties as nanocomposites. Fig. 3(a) shows that the maximum fluorescence intensity emission occurred at 583.79 nm with an excitation wavelength of 545 nm. The optimized MFSNc exhibited a fluorescence intensity 5 times higher than that of MFSNc-F. The magnetic saturation of both MFSNc samples was analyzed using a conventional magnetic hysteresis loop, as shown in Fig. 3(b). The optimized MFSNc demonstrated stronger magnetization than MFSNc-F, with a value of 16.70 emu g^{-1} and a loop area of 0.20 kOe. It also displayed a small curve region (Hc), confirming the material's soft-ferromagnetic nature.[40,42] This behavior is further supported by XPS analysis (Fig. S11), which identifies multiple iron oxide phases, including Fe_3O_4, that play a key role in contributing to the nanocomposite's magnetic properties. The surface area properties of the optimized MFSNc and MFSNc-F were analyzed using a surface area analyzer. Fig. 3(c) presents the nitrogen adsorption–desorption isotherm of both the optimized MFSNc and MFSNc-F, with their profiles identified as type IV adsorption with an H3 hysteresis loop.[37,43] The specific surface areas of the optimized MFSNc and MFSNc-F were 139.45 m^2 g^{-1} and 103.66 m^2 g^{-1}, respectively. The optimal

Table 2 Experimental and predicted results for model validation conducted under the optimum conditions suggested by RSM

Sample	RhB (mg g^{-1})	Fe/Si (g g^{-1})	CTAB (%)	Fl. intensity (a.u.)	Ms (emu g^{-1})	Surface area (m^2 g^{-1})	Desirability	
Optimized	5	0.5	3	566.20	16.70	139.45	0.548	Selected
MFSNc-F	5	0.5	1	116.00	10.83	103.66	N/A	Experimental

 This journal is © The Royal Society of Chemistry 2025

Published on 24 October 2025. Downloaded on 2/11/2026 1:26:59 AM.

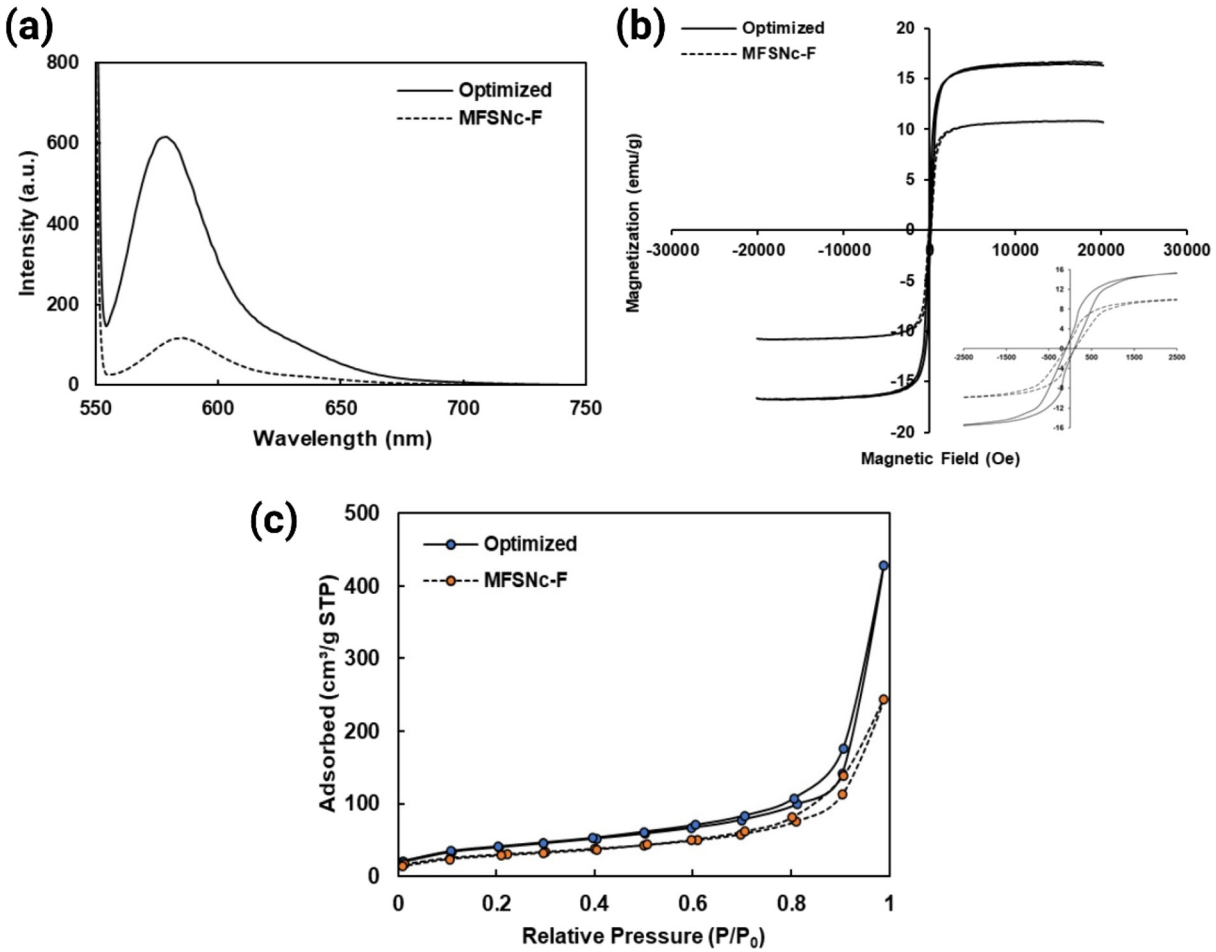

Fig. 3 Comparative analysis of the optimized MFSNc and MFSNc-F, highlighting the differences in the (a) fluorescence intensity, (b) magnetic saturation, and (c) surface area.

results from the optimized MFSNc were suitable for achieving high fluorescence intensity and magnetization. Subsequently, the optimized MFSNc was employed for surface modification with the antibiotic vancomycin to facilitate bacterial detection.

Surface modification of the MFSNc

The RSM-optimized MFSNc was subjected to surface modification, as shown in Fig. 4(a), with the success of the process validated through FTIR analysis. Fig. 4(b) shows the results of FTIR analysis on each sample in the process of surface modification of the MFSNc material prior to conjugation with vancomycin. Overall, the FTIR spectra of the MFSNc samples, the carboxyl-modified MFSNc (MFSNc-COOH), the succinimidyl ester-modified MFSNc (MFSNc-EDC/NHS), and the vancomycin-modified MFSNc (MFSNc-Van), show peaks corresponding to the functional groups of Fe–O, siloxy (Si–O–), and Si–O–Si at wavenumbers of 545 cm^{-1}, 796 cm^{-1}, and 1074 cm^{-1}, respectively. This result is in agreement with a previous study.[37]

The undecylenic acid-modified surface, shown as the spectrum of MFSNc-COOH, showed the appearance of peaks at wavenumbers of 1643 cm^{-1} and 874 cm^{-1}, indicating the C=O stretching bond from the interaction between silica in the MFSNc and the C=O bond in the carboxylic acid. The addition of aliphatic groups originating from undecylenic acid is also seen from the peak at 2927 cm^{-1}, which corresponds to the presence of an alkyl CH_3 group.[39] After the EDC/NHS reaction, the spectrum of MFSNc-EDC/NHS showed a prominent peak at a wavenumber of 1643 cm^{-1} due to the addition of carboxyl groups and the disappearance of the peak at 874 cm^{-1} due to the change of carboxylic acid to succinimidyl ester by the EDC/NHS activator. The broadening of the peak at around 2900–3600 cm^{-1} was plausible due to the overlap between the regions with a stretching C–H bond from the CH_3 group ($–CH_3–CH_2–$) and that of the –OH hydroxyl group. The vancomycin was covalently bound to the MFSNc surface through an amination reaction, which was confirmed by changes in the transmittance peaks in amide groups I and II at wavenumbers of 1500–1640 cm^{-1} and 3400 cm^{-1}, respectively.[11,29]

Detection of *S. aureus* bacteria

MFSNc-Van was observed for its analytical performance as an optical biosensing platform based on changes in the fluo-

Published on 24 October 2025. Downloaded on 2/11/2026 1:26:59 AM.

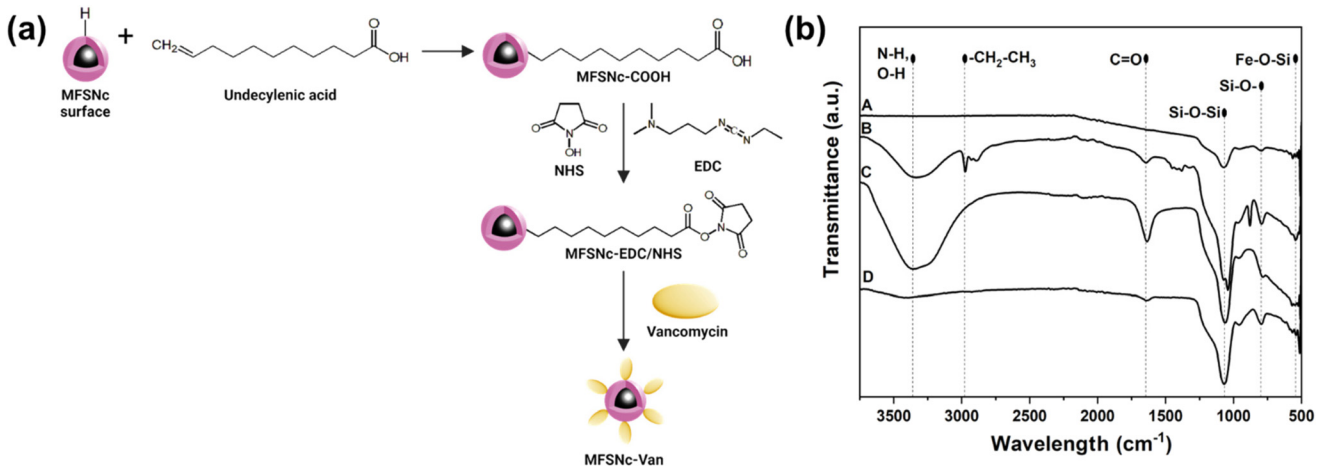

Fig. 4 (a) Schematic illustration of the surface modification process. (b) FTIR spectra of the MFSNc (A), MFSNc-COOH (B), MFSNc-EDC/NHS (C), and MFSNc-Van (D) as results of the surface modification process on the functionalization of the MFSNc.

rescence intensity of the material in the absence and presence of SA bacteria. MFSNc-Van remained stable in PBS for at least 48 hours, with no obvious aggregation or sedimentation, indicating adequate colloidal stability for biosensing applications. The fluorescence intensity of MFSNc-Van was observed in the wavelength range of 550–750 nm at 545 nm excitation.[13,44] The nanocomposites serve as an active surface for vancomycin, enhancing its specificity and allowing efficient bacterial capture. Fig. 5 shows a decrease in the maximum fluorescence intensity of MFSNc-Van at a wavelength of 580 nm after incubation with SA. The initial fluorescence intensity of MFSNc-Van was 42.59 a.u. Upon exposure to SA, the fluorescence intensity of MFSNc-Van decreased significantly to 4.60 a.u. The percentage fluorescence intensity loss ($\%I_{loss}$) that occurred in the MFSNc-Van material was 89.20% after a reaction time of 1 hour. The fluorescence quenching indicates that there is an interaction between the nucleobase of the SA bacterial cell wall and the fluorescent substance. Previous research found that when a substance that has an electron donor excites its electrons and is captured by an acceptor, quenching will occur due to FRET.[30,45] FRET is another quenching mechanism that occurs when two fluorophores are in close proximity (typically <10 nm apart). In our context, the magnetic silica nanoparticle is attached to a fluorophore. If a bacterial target binds to the nanoparticle, the distance between the fluorophore and the bacterial surface changes. FRET occurs when the bacterial binding brings another fluorophore (*e.g.*, a quencher) within close proximity. As a result of the energy transfer between the excited fluorophore and the quencher, the intensity of fluorescence is reduced. Researchers have exploited this phenomenon for biosensing and bacterial detection.[46,47]

The selectivity of MFSNc-Van was observed by detecting other bacteria as a comparison. The observed fluorescence intensity loss when detecting MRSA (methicillin-resistant

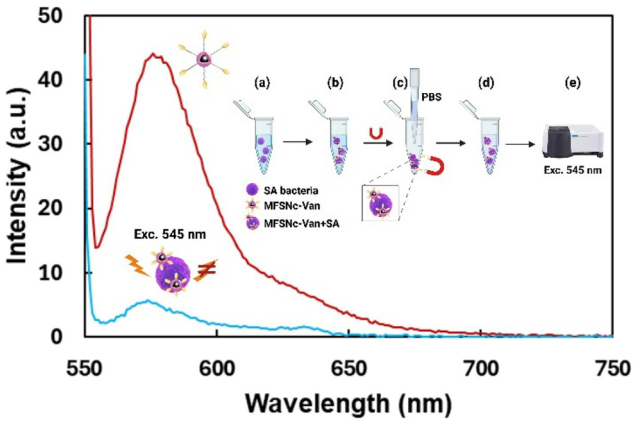

Fig. 5 The fluorescence spectra of MFSNc-Van before (red) and after (blue) the detection of SA at an excitation wavelength of 545 nm. The inset images show the schematic diagram of the detection of *S. aureus* bacteria by MFSNc-Van. SA bacteria in PBS (a), addition of MFSNc-Van to SA (b), separation process using an external magnetic field (c), resuspension of MFSNc-Van + SA in PBS (d), and detection process using a fluorescence spectrometer (e).

Staphylococcus aureus) was lower compared to SA, providing valuable insights into the selectivity (Fig. S12). MRSA strains are particularly concerning due to their resistance to methicillin and other beta-lactam antibiotics. The larger intensity loss in SA suggests that the detection system of MFSNc-Van is more susceptible to SA. The analytical performance of MFSNc-Van in detecting SA bacteria was further investigated. The optimum detection response time was determined by varying the incubation time at a constant concentration of 5 mg mL^{-1} of vancomycin on the MFSNc surface. The detection response time is critical in practical applications as it determines how quickly MFSNc-Van can identify the targets. The $\%I_{loss}$ value increased from 0 to 35 minutes of incubation (Fig. S13). At 25 minutes of incubation time, the

 This journal is © The Royal Society of Chemistry 2025

Published on 24 October 2025. Downloaded on 2/11/2026 1:26:59 AM.

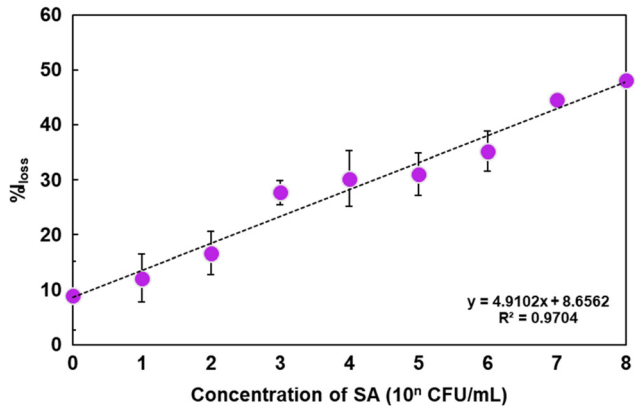

Fig. 6 The correlation between the percentage of fluorescence intensity loss (%I_{loss}) of MFSNc-Van at 580 nm and *S. aureus* bacterial concentrations after 25 minutes of incubation time. All measurements were made in triplicate.

intensity loss reached its highest value. The initial increase in intensity loss suggests that MFSNc-Van efficiently captured the bacteria during the first 25 minutes. The highest intensity loss at 25 minutes indicates the optimal binding of SA bacteria to MFSNc-Van. Vancomycin exhibits high specificity toward Gram-positive bacteria, particularly *Staphylococcus* spp., by binding to D-Ala-D-Ala motifs in their peptidoglycan cell walls.[48] Future designs may include other targeting ligands to enable the selective detection of bacteria with diverse cell wall architectures, such as Gram-negative bacteria.

To determine the sensitivity and LOD value of MFSNc-Van as a biosensing platform, the concentration of SA was varied, ranging from 10^0 to 10^8 CFU mL^{-1}. Using the optimum 25 minutes incubation time, the %I_{loss} value at 580 nm was observed for each SA concentration. Fig. 6 shows that the %I_{loss} value of MFSNc-Van increases linearly with increasing SA concentrations. The highest %I_{loss} value observed was 48.12% at a concentration of 10^8 CFU mL^{-1}, whereas the lowest %I_{loss} was 8.96% at a concentration of 10^0 CFU mL^{-1} SA against the control. The linear regression equation is $y = 4.9102 \log C + 8.6562$, with a correlation coefficient of 0.9704, where y represents the fluorescence intensity of the biosensor and C represents the logarithmic concentration of SA (CFU mL^{-1}). The LOD was calculated using eqn (3). Based on a mean %I_{loss} of 0 for the blank control and a standard deviation (STDb) of 4.04, the LOD was determined to be 5.08 CFU mL^{-1}, representing the lowest reliably detectable concentration of SA within the linear range of 10^0–10^8 CFU mL^{-1}. Overall, these results demonstrate that the MFSNc-Van system offers a highly sensitive and rapid platform for detecting *S. aureus*, with a strong performance under controlled conditions. A comparison with previously reported methods, summarized in Table 3, highlights its competitive advantages in terms of detection limit and incubation time. Moreover, using geothermal silica as a precursor turns industrial waste into useful materials for biosensing applications, providing a sustainable and profitable method.[60] Building on these promising results, future work will focus on extending the application of this biosensor to complex sample matrices such as food extracts and clinical fluids. This will enable further validation of its robustness and practical utility in real-world diagnostic and monitoring scenarios. In parallel, comprehensive biocompatibility assessments, including cytotoxicity studies, residual surfactant quantification, and dye stability evaluation in aqueous media, will be conducted to ensure its safe application in biological and clinical settings.

Table 3 Comparison of different methods for the detection of *S. aureus* bacteria

Methods	Material	Incubation time (min)	LOD (CFU mL^{-1})	Ref.
Electrochemistry	Apt-AgNPs[a]	30	1	49
Luminescence	Multicolor UCNPs[b]	30	25	50
Colorimetric	Au-based aptasensor	45	9	51
Fluorescence	Apt-chimera-MB[c]	80	39	52
Fluorescence	MB-apt-cDNA[d]	40	1.7	53
Fluorescence	Fe_3O_4/CD aptasensor[e]	30	8	54
Electrochemistry	Apt/SPCE/AuNPs[f]	60	0.2	55
Nucleic acid amplification	Functionalized MBs and guide RNA targeting[g]	40	10	56
Dual-mode electrochemistry and fluorescence	CRISPR/Cas12a system	60	5.7 and 133.7	57
Electrochemiluminescence	DL-MOFs[h]	180	2	58
Electrochemistry	Apt/Pt/C-ZIF-8[i]	28	2	59
Fluorescence	MFSNc-Van	25	5.08	This work

[a] Apt-AgNPs: aptamer-conjugated silver nanoparticles. [b] Multicolor UCNPs: multicolor up-conversion nanoparticles. [c] Apt-chimera-MB: functional chimera aptamer and molecular beacon-based sensor. [d] MB-apt-cDNA: aptamer-cDNA-conjugated magnetic beads. [e] Fe_3O_4/CD aptasensor: self-assembled iron oxide and carbon dot nanomaterial-based aptasensor. [f] Apt/SPCE/AuNPs: aptamer-modified gold nanoparticles integrated into screen-printed carbon electrodes. [g] Functionalized MBs and guide RNA targeting: magnetic beads functionalized with SA-specific antibodies and a CRISPR/Cas12a system as guide RNA. [h] DL-MOFs: dual-ligand metal–organic frameworks. [i] Apt/Pt/C-ZIF-8: aptamer-based ZIF8-derived carbon decorated with platinum nanoparticle hybrids.

Published on 24 October 2025. Downloaded on 2/11/2026 1:26:59 AM.

Conclusions

This study successfully developed a magnetic fluorescent nanosensor using modified sustainable silica from geothermal sources for the sensitive detection of SA bacteria. The MFSNc was synthesized using the sol–gel method, with sustainable silica as the precursor, an iron oxide core, and rhodamine B as a fluorescent dye. The optimization of MFSNc synthesis was achieved using the Box–Behnken Design Response Surface Methodology (BBD-RSM). The use of rhodamine B, Fe/Si, and CTAB influenced the fluorescence intensity, magnetic saturation, and surface area of the MFSNc material. RSM identified the optimal composition as 0.5 g g^{-1} Fe/Si, 3% CTAB, and 5 mg g^{-1} rhodamine B. Validation experiments confirmed the RSM predictions, resulting in a nanocomposite with a maximum fluorescence intensity of 566.20 a.u., a magnetic saturation of 16.70 emu g^{-1}, and a specific surface area of 139.45 m^2 g^{-1}.

The RSM-optimized MFSNc was further modified with vancomycin and used as a biosensing platform. A linear correlation between the $\%I_{loss}$ value of MFSNc-Van and SA concentration was observed in the range of 10^0–10^8 CFU mL^{-1}, with a limit of detection as low as 5.08 CFU mL^{-1} and an incubation time of 25 minutes. This study underscores the design and synthesis of a bifunctional magnetic–fluorescent iron oxide silica core/shell nanocomposite, highlighting its potential applications in clinical diagnostics, food safety, and monitoring environmental samples for SA contamination.

Author contributions

Falah Azizah Elmaria: methodology, investigation, data curation, formal analysis, and writing – original draft. Fauzan Aulia: resources, formal analysis, investigation, and validation. Shaimah Rinda Sari: writing – review & editing, data curation, formal analysis, visualization, validation, and investigation. Sudiyarmanto: data curation, formal analysis, resources, investigation, and validation. Abdi Wira Septama: resources, formal analysis, investigation, and validation. Yuni Kusumastuti: resources, formal analysis, investigation, and validation. Himawan Tri Bayu Murti Petrus: validation, funding acquisition, supervision, conceptualization, and project administration. S. N. Aisyiyah Jenie: writing – review & editing, validation, funding acquisition, supervision, conceptualization, methodology, and project administration.

Conflicts of interest

The authors declare that they have no known competing financial interests or personal relationships that could have appeared to influence the work reported in this paper.

Data availability

The data supporting this article have been included as part of the supplementary information (SI). Supplementary information is available. See DOI: https://doi.org/10.1039/d5nr01610j.

Acknowledgements

The authors would like to acknowledge the financial support from the JFS SEA-EU/NAPARBA Project Grant No. SEA-EUROPE JFS19ST-117, the National Research and Innovation Agency (BRIN) and the Indonesian Endowment Fund for Education (LPDP) through the Riset & Inovasi untuk Indonesia Maju (RIIM) Grant No. 19/II.7/HK/2023. This study was also partly funded by the Indonesian Endowment Fund for Education (LPDP) on behalf of the Indonesian Ministry of Education, Culture, Research and Technology and managed under the INSPIRASI Program (Grant No. 6637/E3/KL.02.02/2023 and 13577/UN.1P/DPU/HK.08.00/2023). S. N. A. J. is the main contributor of this manuscript.

References

1 S. N. A. Jenie, A. Ghaisani, Y. P. Ningrum, A. Kristiani, F. Aulia and H. T. M. B. Petrus, *AIP Conf. Proc.*, 2018, **2026**, 020008.
2 L. Y. Gomez-Zamorano, E. Vega-Cordero and L. Struble, *Constr. Build. Mater.*, 2016, **115**, 269–276.
3 D. F. Fitriyana, H. Suhaimi, Sulardjaka, R. Noferi and W. Caesarendra, *Springer Proceedings in Physics*, 2020, pp. 51–59.
4 Y. Kusumastuti, F. Larasati, D. R. Gunawan, M. Najmina, N. R. E. Putri, H. T. B. M. Petrus and M. Kobayashi, *IOP Conf. Ser.:Mater. Sci. Eng.*, 2019, **543**, 012028.
5 F. D. S. Bruckmann, F. B. Nunes, T. D. R. Salles, C. Franco, F. C. Cadoná and C. R. B. Rhoden, *Magnetochemistry*, 2022, **8**, 131.
6 H. Abdolmohammad-Zadeh, S. Hassanlouei and M. Zamani-Kalajahi, *RSC Adv.*, 2017, **7**, 23293–23300.
7 K. Cendrowski, P. Sikora, B. Zielinska, E. Horszczaruk and E. Mijowska, *Appl. Surf. Sci.*, 2017, **407**, 391–397.
8 F. A. Elmaria and S. N. A. Jenie, *J. Kim. Ter. Indones.*, 2021, **23**, 49–54.
9 I. Yildiz, *Nanotechnol. Rev.*, 2016, **5**, 331–340.
10 F. Mohandes, H. Dehghani, S. Angizi, A. Ramedani, B. Dolatyar, M. R. Farani, K. Müllen and A. Simchi, *J. Magn. Magn. Mater.*, 2022, **561**, 169686.
11 J. Yang, J. Lee, J. Kang, C.-H. Chung, K. Lee, J.-S. Suh, H.-G. Yoon, Y.-M. Huh and S. Haam, *Nanotechnology*, 2008, **19**, 075610.
12 N. O. Sifana, Melyna, N. L. W. Septiani, A. W. Septama, R. V. Manurung, B. Yuliarto and S. N. A. Jenie, *Spectrochim. Acta, Part A*, 2024, **307**, 123643.
13 S. N. A. Jenie, Y. Kusumastuti, F. S. H. Krismastuti, Y. M. Untoro, R. T. Dewi, L. Z. Udin and N. Artanti, *Sensors*, 2021, **21**, 881.

 This journal is © The Royal Society of Chemistry 2025

Published on 24 October 2025. Downloaded on 2/11/2026 1:26:59 AM.

14 M. Rajasekar, *J. Mol. Struct.*, 2021, **1235**, 130232.
15 W. Wang, S. Liu, C. Li, Y. Wang and C. Yan, *Talanta*, 2018, **182**, 306–313.
16 A. Yadav, C. Rao, N. C. Verma, P. M. Mishra and C. K. Nandi, *Mol. Imaging*, 2020, **19**, 1536012120969477.
17 B. Dubertret, M. Calame and A. J. Libchaber, *Nat. Biotechnol.*, 2001, **19**, 365–370.
18 Z. Huang, J. Peng, J. Han, G. Zhang, Y. Huang, M. Duan, D. Liu, Y. Xiong, S. Xia and W. Lai, *Food Chem.*, 2019, **276**, 333–341.
19 M. Kavruk, O. Celikbicak, V. C. Ozalp, B. A. Borsa, F. J. Hernandez, G. Bayramoglu, B. Salih and M. Y. Arica, *Chem. Commun.*, 2015, **51**, 8492–8495.
20 F. D. Lowy, *N. Engl. J. Med.*, 1998, **339**, 520–532.
21 S. S. Samani, A. Khojastehnezhad, M. Ramezani, M. Alibolandi, F. T. Yazdi, S. A. Mortazavi, Z. Khoshbin, K. Abnous and S. M. Taghdisi, *Talanta*, 2021, **226**, 122168.
22 B. Jubeh, Z. Breijyeh and R. Karaman, *Molecules*, 2020, **25**, 2888.
23 W. A. Fitri, L. Sururoh and S. N. A. Jenie, *AIP Conf. Proc.*, 2019, **2175**, 020080.
24 Y. Huang, P. Li, R. Zhao, L. Zhao, J. Liu, S. Peng, X. Fu, X. Wang, R. Luo, R. Wang and Z. Zhang, *Biomed. Pharmacother.*, 2022, **151**, 113053.
25 M. M. Abdelaziz, A. Hefnawy, A. Anter, M. M. Abdellatif, M. A. F. Khalil and I. A. Khalil, *ACS Omega*, 2022, **7**, 30161–30170.
26 H. Rong, T. Gao and X. Zhang, *Compos. Commun.*, 2020, **20**, 100368.
27 Z. Tavakoli, B. Rasekh, F. Yazdian, A. Maghsoudi, M. Soleimani and J. Mohammadnejad, *Int. J. Biol. Macromol.*, 2019, **135**, 600–608.
28 B. Ba Mohammed, A. Hsini, Y. Abdellaoui, H. Abou Oualid, M. Laabd, M. El Ouardi, A. Ait Addi, K. Yamni and N. Tijani, *J. Environ. Chem. Eng.*, 2020, **8**, 104419.
29 D. R. Pinheiro, R. D. F. Neves and S. P. A. Paz, *Microporous Mesoporous Mater.*, 2021, **323**, 111250.
30 D. A. Widyasari, A. Kristiani, A. Randy, R. V. Manurung, R. T. Dewi, A. S. Andreani, B. Yuliarto and S. N. A. Jenie, *RSC Adv.*, 2022, **12**, 21582–21590.
31 D. A. Widyasari, D. Julyansyah, A. Kristiani, B. A. Widyaningrum, H. T. B. M. Petrus, R. V. Manurung and S. N. A. Jenie, *AIP Conf. Proc.*, 2021, **2382**, 030009.
32 S. N. A. Jenie, Z. Du, S. J. P. McInnes, P. Ung, B. Graham, S. E. Plush and N. H. Voelcker, *J. Mater. Chem. B*, 2014, **2**, 7694–7703.
33 L. Chen and J. Zhang, *J. Biosens. Bioelectron.*, 2012, (S11), 005.
34 D. R. B. Albano, K. Shum, J. A. Tanner and Y. S. Fung, *Proc. IMCS*, 2018, **2018**, 211–213.
35 X. Wu and Z. Nan, *Mater. Chem. Phys.*, 2019, **227**, 302–312.
36 A. Pongprom, N. Chansud, S. Sa-nguanprang, S. Jullakan and O. Bunkoed, *Microchem. J.*, 2023, **187**, 108389.
37 M. Y. Maulana, R. Raissa, A. Nurrudin, A. S. Andreani, M. Angelina, N. L. W. Septiani, B. Yuliarto and S. N. A. Jenie, *Nanotechnology*, 2024, **35**, 205702.
38 K. Koc, B. Karakus, K. Rajar and E. Alveroglu, *Superlattices Microstruct.*, 2017, **110**, 198–204.
39 S. V. Stolyar, R. N. Yaroslavtsev, A. V. Tyumentseva, S. V. Komogortsev, E. S. Tyutrina, A. T. Saitova, Y. V. Gerasimova, D. A. Velikanov, M. V. Rautskii and R. S. Iskhakov, *J. Phys. Chem. C*, 2022, **126**, 7510–7516.
40 F. A. Elmaria, F. Aulia, L. N. Hidayati, A. Kristiani, Sudiyarmanto, Y. Kusumastuti, S. N. A. Jenie and H. T. M. B. Petrus, *J. Sol-Gel Sci. Technol.*, 2024, **110**, 27–36.
41 M. Tajabadi, I. Rahmani, S. M. Mirkazemi and H. Goran Orimi, *Adv. Powder Technol.*, 2022, **33**, 103366.
42 K. Kohaku, M. Inoue, H. Kanoh, T. Taniguchi, K. Kishikawa and M. Kohri, *ACS Appl. Polym. Mater.*, 2020, **2**, 1800–1806.
43 S. N. A. Jenie, A. Kristiani, Sudiyarmanto, D. S. Khaerudini and K. Takeishi, *J. Environ. Chem. Eng.*, 2020, **8**, 103912.
44 S. N. A. Jenie, F. S. H. Krismastuti, Y. P. Ningrum, A. Kristiani, M. D. Yuniati, W. Astuti and H. T. B. M. Petrus, *Mater. Express*, 2020, **10**, 258–266.
45 Y. Wang, C. Jiang, G. Wen, X. Zhang, Y. Luo, A. Qin, A. Liang and Z. Jiang, *Luminescence*, 2015, **31**, 972–977.
46 Y. Si, C. Grazon, G. Clavier, J.-F. Audibert, B. Sclavi and R. Méallet-Renault, *Photochem. Photobiol. Sci.*, 2022, **21**, 1249–1255.
47 A. K. Verma, A. Noumani, A. K. Yadav and P. R. Solanki, *Diagnostics*, 2023, **13**, 1375.
48 F. Wang, H. Zhou, O. P. Olademehin, S. J. Kim and P. Tao, *ACS Omega*, 2018, **3**, 37–45.
49 A. Abbaspour, F. Norouz-Sarvestani, A. Noori and N. Soltani, *Biosens. Bioelectron.*, 2015, **68**, 149–155.
50 S. Wu, N. Duan, Z. Shi, C. Fang and Z. Wang, *Anal. Chem.*, 2014, **86**, 3100–3107.
51 J. Yuan, S. Wu, N. Duan, X. Ma, Y. Xia, J. Chen, Z. Ding and Z. Wang, *Talanta*, 2014, **127**, 163–168.
52 R. Cai, F. Yin, Z. Zhang, Y. Tian and N. Zhou, *Anal. Chim. Acta*, 2019, **1075**, 128–136.
53 R. Cai, F. Yin, H. Chen, Y. Tian and N. Zhou, *Microchim. Acta*, 2020, **187**, 304.
54 F. Cui, J. Sun, J. de Dieu Habimana, X. Yang, J. Ji, Y. Zhang, H. Lei, Z. Li, J. Zheng, M. Fan and X. Sun, *Anal. Chem.*, 2019, **91**, 14681–14690.
55 S. Soleimani, T. A. Bruce-Tagoe, N. Ullah, M. G. Rippy, H. G. Spratt and M. K. Danquah, *Anal. Bioanal. Chem.*, 2024, **416**, 4619–4634.
56 Y. Ma, H. Wei, Y. Wang, X. Cheng, H. Chen, X. Yang, H. Zhang, Z. Rong and S. Wang, *J. Hazard. Mater.*, 2024, **465**, 133494.
57 H. Gao, H. Zhang, X. Qi, M. Miao, L. Que, X. Gu, D. Chang and H. Pan, *Talanta*, 2025, **282**, 127013.
58 X. Wang, Z. Yan, F. Zhang, J. Xia and Z. Wang, *Chem. Eng. J.*, 2025, **512**, 162433.
59 X. Jiang, Z. Lv, X. Chen and C. Rao, *Microchem. J.*, 2025, **209**, 112627.
60 S. N. A. Jenie, A. Kristiani, R. R. Widjaya, Y. Kusumastuti, P. Prihutami, W. Astuti, F. Anggara, S. R. Sari, Y. G. Wibowo and H. T. B. M. Petrus, *Mater. Today Commun.*, 2025, **43**, 111635.